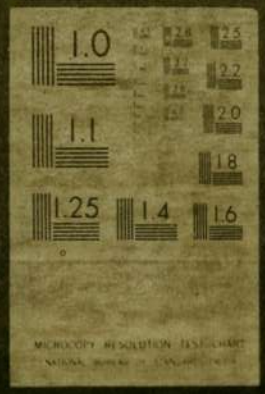

CO-3067(2)-2

Ccc-

MASTER

KINEMATIC DISTRIBUTIONS FOR ELECTRON PAIR PRODUCTION BY MUONS*

Ralph Linsker

Department of Physics
Columbia University
New York, New York 10027

and

Institute for Space Studies
Goddard Space Flight Center
National Aeronautics and Space Administration
New York, New York 10025

* Research supported in part by the National Aeronautics and Space Administration and the U. S. Atomic Energy Commission.

ABSTRACT

Cross sections and kinematic distributions for the trident production process $\mu^{\pm} + Z \rightarrow \mu^{\pm} + e^{-} + e^{+} + Z$ (with Z = p and Fe) are given for beam energies of 100-300 GeV at fixed $(e^{-}e^{+})$ masses from 5 to 15 GeV. This process is interesting as a test of quantum electrodynamics at high energies, and in particular as a test of the form of the photon propagator at large timelike (four-momentum)^2. For this purpose, it is desirable to impose kinematic cuts that favor those Bethe-Heitler graphs which contain a timelike photon propagator. It is found that there are substantial differences between the kinematic distributions for the full Bethe-Heitler matrix element (which involves four graphs) and the distributions for the two timelike-photon graphs alone; these differences can be exploited in the selection of appropriate kinematic cuts. The competing virtual Compton process (for Z = p) has been estimated on the basis of a simple model; its cross section is at least two orders of magnitude smaller than the Bethe-Heitler cross sections of interest, at the energies and $(e^{-}e^{+})$ masses considered.

I. INTRODUCTION

In this paper cross sections and distributions for the trident process

$$\mu^{\pm} + Z \rightarrow \mu^{\pm} + e^{-} + e^{+} + Z \qquad (1.1)$$

are calculated to lowest order of the conventional quantum electrodynamics for the cases of elastic scattering off a proton and coherent scattering off a spin-0 nucleus. This process, as well as the essentially identical reaction

$$e^{\pm} + Z \rightarrow e^{\pm} + \mu^{-} + \mu^{+} + Z \qquad (1.2)$$

and the related process

$$\ell^{\pm} + Z \rightarrow \ell^{\pm} + \ell^{-} + \ell^{+} + Z \qquad (1.3)$$

(where $\ell = \mu$ or e) are of interest because they are sensitive to possible modifications in lepton electrodynamics at high energies. In particular, we are interested in facilitating the detection of possible deviation from conventional QED, especially in connection with the mass spectrum of the lepton pair produced in processes (1.1) or (1.2). Such a deviation could be due, for example, to a modification of the photon propagator along the lines of the Lee-Wick "heavy photon pole" model.[1,2]

In the Lee-Wick theory, the possibility of replacing the conventional photon field amplitude A_μ by a complex amplitude $A_\mu + iB_\mu$, where iB_μ is anti-Hermitian, is studied. Such a modification (coupled

with the introduction of a massive indefinite-metric fermion field) yields finite results for calculations of observable quantities in hadron as well as lepton electrodynamics. Total cross sections for the resonant process

$$\ell^{\pm} + Z \rightarrow \ell^{\pm} + Z' + B^{0} \qquad (1.4)$$

($B^0 \rightarrow$ leptons or hadrons)

where $\ell = \mu$ or e, and B^0 is the massive indefinite-metric boson associated with the amplitude B_μ, have been given in previous papers[3,4] (I).

The Bethe-Heitler diagrams for process (1.1), in which only one photon is exchanged with the nucleon or nucleus, are given in Fig. 1 (for incident μ^-). There are four such graphs, corresponding to the interaction with the nucleon or nucleus Z occurring at any of the positions (a)-(d). The competing virtual Compton graph is indicated generally in Fig. 2(a). The virtual Compton cross section for scattering off protons is calculated in this paper using a simple model of the hadronic interaction. It is found to be two to four orders of magnitude less than the corresponding Bethe-Heitler cross sections of interest.

The main effect of the Lee-Wick (or similar) modification upon processes (1.1) and (1.2) is to enhance the singly-differential cross section $\frac{d\sigma}{dv}$ in the vicinity of the B^0 resonance, where v is the $(\text{mass})^2$ of the timelike virtual photon. The enhancement of that part of the cross section which involves only diagrams (a) and (b) of Fig. 1 (i.e., the graphs which contain a timelike photon propagator), is given approximately by the factor[1,2] $m_B^4/(m_B^2 - v)^2$, provided v is not $\cong m_B^2$.

Thus if $m_B = 20$ GeV, for example, an 80% enhancement should be seen at $\sqrt{v} = 10$ GeV.

However, if one measures $\frac{d\sigma}{dv}$ (integrated over all kinematic configurations consistent with fixed v), it will be seen that this enhancement effect will generally be nearly totally obscured by the much larger contribution from those diagrams [see Fig. 1, cases (c) and (d)] in which all photon propagators are spacelike. The reason for this is simply that if no additional kinematic constraints are imposed, the spacelike photon joining leptonic vertices in cases (c) and (d) of Fig. 1 can be much closer to the light cone than can the timelike photon in cases (a) and (b), for $\sqrt{v}$ in the region of interest ($\gtrsim 10$ GeV). Consequently, we shall also be concerned with the kinematic distributions for processes (1.1) and (1.2), and with the types of kinematic cuts that can be made to increase the relative contribution of the timelike graphs. This information is useful as a guide for experimental searches for possible deviations of the timelike photon propagator from the predictions of conventional QED. The distributions are obtained efficiently by a binning procedure incorporated within a modified Monte Carlo integration scheme.

In Section II, the matrix element (corresponding to the diagrams of Fig. 1) is given for process (1.1) [or (1.2) with the exchange $\mu \longrightarrow e$].

Section III gives the differential cross section expressed in a convenient set of variables. Section IV describes the phase space integration and numerical methods used. In Section V the contribution of the virtual Compton graphs is discussed. In Section VI the results are presented and discussed. In Appendix A, expressions for the relevant dot products and related quantities are derived in terms of the variables defined in Section III. Appendix B gives the limit of integration for each variable, and describes the method used for incorporating kinematic cuts into the integration scheme.

II. MATRIX ELEMENT

A. Leptonic Part

The matrix element corresponding to the four Bethe-Heitler diagrams of Fig. 1 is[5]

$$\mathfrak{M} = K_\sigma V_\sigma \tag{2.1}$$

$$K_\sigma = T_\sigma + S_\sigma ; \tag{2.2}$$

where

$$T_\sigma = ie^3 v^{-1} \bar{u}_2 \gamma_\lambda v_3 \bar{u}_1 \left[D_a^{-1} \gamma_\lambda \left(-q \cdot \gamma \gamma_\sigma + 2k_\sigma \right) + D_b^{-1} \left(\gamma_\sigma q \cdot \gamma + 2k_{1\sigma} \right) \gamma_\lambda \right] u \tag{2.3}$$

is the contribution of the "timelike" diagrams (a) and (b) of Fig. 1, and

$$S_\sigma = -ie^3 D^{-1} \bar{u}_1 \gamma_\lambda u \, \bar{v}_2 \left[D_c^{-1} \left(\gamma_\sigma q \cdot \gamma + 2k_{2\sigma} \right) \gamma_\lambda - D_d^{-1} \gamma_\lambda \left(q \cdot \gamma \gamma_\sigma + 2k_{3\sigma} \right) \right] v_3 \tag{2.4}$$

is the contribution of the "spacelike" diagrams (c) and (d). Here k, k_1, k_2, k_3 are the respective four-momenta of the incoming and outgoing μ^-, and the e^- and e^+ (see Fig. 1), satisfying $k^2 = k_1^2 = -m_\mu^2$ and $k_2^2 = k_3^2 = -m_e^2$; and $q = p' - p$ where p and p' are the respective initial and final four-momenta of the nucleon or nucleus Z, with $p^2 = p'^2 = -M^2$. The propagator denominators are

$$\begin{aligned} v &= -(k_2 + k_3)^2 \\ D &= (k - k_1)^2 \\ D_a &= q^2 - 2k \cdot q \\ D_b &= q^2 + 2k_1 \cdot q \\ D_c &= q^2 + 2k_2 \cdot q \\ D_d &= q^2 + 2k_3 \cdot q \end{aligned} \tag{2.5}$$

The spinors corresponding to the particles of momentum k, k_1, and k_2, and to the antiparticle of momentum k_3, are denoted u, u_1, u_2, and v_3 respectively; they are normalized so that $\bar{u}u = \bar{u}_1 u_1 = 2m_\mu$ and $\bar{u}_2 u_2 = -\bar{v}_3 v_3 = 2m_e$.

B. Hadronic Part

The hadronic vertex and photon propagator q in Fig. 1 contribute the factor V_σ. The V_σ used here are identical to the corresponding factors of paper I. For elastic scattering off a free proton, the dipole fit[6] is sufficiently accurate for our purposes:

$$F_1(q^2) = G[1 + \kappa(1 + 4M^2/q^2)^{-1}] ,$$

$$F_2(q^2) = \frac{1}{2} G\kappa(1 + q^2/4M^2)^{-1} , \qquad (2.6)$$

where

$$G = (1 + q^2/0.71)^{-2} , \quad q \text{ in GeV} ; \qquad (2.7)$$

and

$$\kappa = 1.7928 .$$

Then

$$V_\sigma = (ie/q^2)\bar{u}_{p'}[F_1\gamma_\sigma + \tfrac{1}{2} i F_2 M^{-1}(\gamma_\sigma\gamma_\beta - \gamma_\beta\gamma_\sigma)q_\beta]u_p , \qquad (2.8)$$

where u_p and $u_{p'}$ are the initial and final-state proton spinors, satisfying $\bar{u}_p u_p = \bar{u}_{p'} u_{p'} = 2M$.

For coherent scattering off a spin-0 nucleus of charge Z, we have

$$V_\sigma = (eZ/q^2)(p + p')_\sigma F(q^2) . \qquad (2.9)$$

We assume for the nucleus a Fermi charge distribution in the Breit frame[7] ($q_0 = 0$)

$$\rho_F(r) \propto [1 + \exp[(r - r_0)/c]]^{-1} \qquad (2.10)$$

with

$$r_0 = (1.18A^{1/3} - 0.48) \text{ fermi}, \quad c = 0.55 \text{ fermi}, \qquad (2.11)$$

and ρ_F normalized such that $\int \rho_F(r) d^3r = 1$. The form factor is given by (see paper I)

$$F(q^2) = [\int \rho_F(r) e^{i\vec{q}\cdot\vec{r}} d^3r]\, \theta(0.25\ \text{GeV}^2 - q^2) \qquad (2.12)$$

integrated in the Breit frame, where $\theta(x) = 1$ for $x \geq 0$ and $\theta(x) = 0$ for $x < 0$. We have thus imposed the arbitrary but convenient cutoff[8] $q^2 \leq 0.25\ \text{GeV}^2$.

For each of the above choices for V_σ, we define[5]

$$H_{\sigma\tau} = \frac{q^4}{e^2} \Sigma_h' V_\sigma V_\tau^{\circledast} , \qquad (2.13)$$

where Σ_h' denotes the average over initial and summation over final spins (if any). [For any four-vector $a = (\vec{a}, ia_0)$, we define $a^{\circledast} = (\vec{a}^*, ia_0^*)$, where * denotes complex conjugation.] Since $H_{\sigma\tau} = H_{\tau\sigma}$ and $q_\sigma H_{\sigma\tau} = 0$, we may write

$$H_{\sigma\tau} = H_1\left(\delta_{\sigma\tau} - \frac{q_\sigma q_\tau}{q^2}\right) + \frac{H_2}{M^2}\left(p_\sigma - \frac{p\cdot q}{q^2} q_\sigma\right)\left(p_\tau - \frac{p\cdot q}{q^2} q_\tau\right) . \qquad (2.14)$$

Thus, for elastic scattering off protons, we have

$$H_1 = q^2\left(F_1 + 2F_2\right)^2$$

$$H_2 = 4\left(F_1^2 M^2 + F_2^2 q^2\right) ; \qquad (2.15)$$

and for coherent scattering off iron,

$$H_1 = 0$$

$$H_2 = (2MZF)^2 \quad . \tag{2.16}$$

III. DIFFERENTIAL CROSS SECTION

The differential cross section for process (1.1), assuming the beam to be unpolarized, and summing over spins of final-state particles, is given by[5]

$$d^8\sigma = \frac{d^3p' d^3k_1 d^3k_2 d^3k_3}{4^7 \pi^8 M |\vec{k}|_{lab} p_0' k_{10} k_{20} k_{30}}$$

$$\times \delta^{(4)}(k - k_1 - k_2 - k_3 - q) \Sigma_\ell' \Sigma_h' |\mathfrak{M}|^2 \tag{3.1}$$

where Σ_ℓ' denotes the average over initial and summation over final lepton spins. To simplify the six-fold numerical integrations (discussed in Section IV), it will prove convenient to express $d^8\sigma$ in the following set of variables. We define

$$\begin{aligned} t &= q^2 \\ u_1 &= k \cdot q \\ u_2 &= 2(k - k_1) \cdot q \\ u_3 &= (k - k_1) \cdot (k_2 - k_3) \quad . \end{aligned} \tag{3.2}$$

$\phi_{p'}$ = azimuthal angle from an arbitrary axis to $\vec{p}'$ about polar axis $\vec{k}$ in the lab frame ($\vec{p} = 0$), ϕ_{1A} = azimuthal angle from $\vec{p}$ to $\vec{k}_1$ about polar axis $\vec{k}$ in the frame $\vec{k} = \vec{q}$ (called frame "A"), and ϕ_{3B} = azimuthal angle from $\vec{k}$ to $\vec{k}_3$ about polar axis $\vec{q}$ in the frame $\vec{k} - \vec{k}_1 = \vec{q}$ (called frame "B").

Then

$$d^8\sigma = \frac{\alpha^4}{64\pi^4 M^2 E_{lab}} \left[\frac{dt\, du_1\, d\phi_p'}{2M E_{lab}}\right] \left[\frac{dv\, du_2\, d\phi_{1A}}{(4u_1^2 + m_\mu^2 t)^{\frac{1}{2}}}\right]$$

$$\times \left[\frac{du_3\, d\phi_{3B}}{/s}\right] \left[\frac{L_{\sigma\tau} H_{\sigma\tau}}{t^2}\right] \qquad (3.3)$$

where

$$L_{\sigma\tau} = (4\pi\alpha)^{-3} \Sigma_l' K_\sigma K_\tau^{\circledast} \qquad (3.4)$$

$$= \qquad (2t - u_2)^2 + 4tv \qquad (3.5)$$

and where the four brackets are equal, respectively, to

$$\left[d^3p'/E_0'\right]_{lab}, \left[d^3k_1/k_{10}\right]_A,$$

$$\left[d^3k_2 d^3k_3 \delta^{(4)}(k + k_1 + k_2 - k_3 - q)/k_{20}k_{30}\right]_B,$$

and

$$\left[(4\pi\alpha)^{-4} \Sigma_l' \Sigma_h' |\mathcal{M}|^2\right].$$

Since $q_\sigma L_{\sigma\tau} = q_\tau L_{\sigma\tau} = 0$, Eq. (2.14) implies

$$L_{\sigma\tau} H_{\sigma\tau} = H_1 L_{\sigma\sigma} + \frac{H_2}{M^2} p_\sigma L_{\sigma\tau} p_\tau . \qquad (3.6)$$

$L_{\sigma\sigma}$ and $p_\sigma L_{\sigma\tau} p_\tau$ are evaluated in invariant form, using Veltman's symbolic manipulation program SCHOONSCHIP[9] to perform the tedious trace calculations. (It should be noted that the expression for $L_{\sigma\sigma}$ is not needed in the case of coherent scattering, since $H_1 = 0$.) The resulting expressions for $L_{\sigma\tau}$ and $p_\sigma L_{\sigma\tau} p_\tau$ are composed of dot products involving the four-vectors k, k_1, k_2, k_3, q, and p (the latter appears only in $p_\sigma L_{\sigma\tau} p_\tau$). These dot products are given in Appendix A as functions of the seven variables v, t, u_1, u_2, u_3, ϕ_{1A}, and ϕ_{3B}. In the next section use is made of the fact that only $k_1 \cdot p$, $k_2 \cdot p$, and $k_3 \cdot p$ depend upon ϕ_{1A}, and only $k_2 \cdot p$, $k_3 \cdot p$, $k \cdot k_2$, $k_1 \cdot k_2$, $k \cdot k_3$, and $k_1 \cdot k_3$ depend upon ϕ_{3B}. The computation time is enormously reduced by factoring out this ϕ_{1A} and ϕ_{3B} dependence.

IV. PHASE SPACE INTEGRATION

In this section the procedure used to integrate the differential cross section over all variables (except v, the square of the invariant mass of the electron pair) is described, and the lab variables over which binning is performed are given.

A. Choice of Integration Variables

The kinematic limits for the variables defined thus far (i.e., t, u_1, u_2, u_3, ϕ_{3B}, and ϕ_{1A}) are given in Appendix B. Two primary advantages have been gained by introducing these variables, rather than attempting to integrate the differential cross section in the lab frame. First, the fact that the integrand depends in a very simple way upon ϕ_{3B} and ϕ_{1A} enables a considerable reduction in computing time, as mentioned in the previous section. Second, if the integrations were performed in the lab frame, special procedures would be required for choosing the points of evaluation in such a way as to take account of the relativistic peaking of the integrand in the forward direction. This difficulty is eliminated by doing several of the integrations in the CM frames of selected subsets of particles. (Frame "A" is the CM frame of k_1, k_2, and k_3; frame "B", of k_2 and k_3.)

However, the integrand is still not sufficiently smooth in these variables to perform a Monte Carlo integration of sufficient accuracy. This is because several of the propagator denominators can attain very small values in certain kinematic regions. It should be noted that each of the denominators (D, D_a, D_b, D_c, D_d, and t) is linear in v, t, u_1, u_2, and u_3, and is independent of ϕ_{3B} and ϕ_{1A} [see Eq. (A. 15)]. This fact helps to make it convenient to transform to a new set of integration variables, chosen so that the new integrand (including the Jacobian) is moderately smooth in the new variables. This is of course equivalent to optimizing the placement of the points of evaluation of the integrand, to take account of rapid variations in the original integrand (resulting both from the propagator denominators and the hadronic form factors).

The following transformation has proved useful in this regard, although a somewhat different choice could also have been made:

$$x_1 = \begin{cases} \int_t^\infty G(t')^2\, dt', & \text{for scattering off protons} \\ [I'(0) - I'(t)]^{1/2}, & \text{for scattering off nucleus.} \end{cases}$$

$$x_2 = u_1$$

$$x_3 = \ln\left(\frac{D}{D_b}\right) = \ln\left(\frac{-v - t + u_2}{t + 2u_1 - u_2}\right)$$

$$x_4 = \frac{1}{\sqrt{\delta}} \ln\left(\frac{D_c}{D_d}\right) = \frac{1}{\sqrt{\delta}} \ln\left(\frac{u_2 + 2u_3}{u_2 - 2u_3}\right) \qquad (4.1)$$

where δ is given by Eq. (3.5),

$$I'(t) = \int_t^\infty F(t')^2\, dt' \ .$$

G is the dipole form factor [Eq. (2.7)], and F is the Fermi form factor [Eq. (2.12)]. In the case of coherent scattering, I′ is tabulated as a function of t, and the conversion between t and I′ is accomplished by interpolating in this (sufficiently dense) table. (See paper I and Ref. 7.)

The rationale of the transformation (4.1) is as follows. The Jacobian for the mapping $t \to x_1$ reduces the peaking at small t due to the hadronic interaction factor V_τ. Next,

$$dx_3 = (2u_1 - v)(D D_b)^{-1} du_2 \tag{4.2}$$

results in the complete elimination of the D^{-1} and D_b^{-1} factors in the cross terms between diagram (b) and either of diagrams (c) and (d), in Fig. 1. The effect of this transformation upon the entire factor $L_{\sigma\tau} H_{\sigma\tau}$ is more complicated, but a reasonable smoothing of the integrand results. The $u_3 \to x_4$ transformation, whose Jacobian is given by

$$dx_4 = \frac{u_2}{D_c D_d \sqrt{\delta}} du_3 \tag{4.3}$$

similarly smooths (in part) the u_3 variation due to D_c and D_d. The denominators v and D_a require no special treatment, since $|D_a| > v$ and we are interested in the case of large v.

B. Numerical Method

We obtain the singly-differential cross section $d\sigma/dv$, and its distributions in lab energy, angle and related variables, by a modified Monte Carlo method. The six-dimensional integration region (in the

variables $x_{1\to4}$, ϕ_{3B}, and ϕ_{1A}, with the outermost integration being x_1 and the innermost, ϕ_{1A}) is partitioned into

$$N = \prod_{i=1}^{6} N_i \tag{4.4}$$

rectangular boxes, corresponding to N_j equally-spaced intervals along the x_j axis ($j=1\to4$), N_5 along ϕ_{3B}, and N_6 along ϕ_{1A}. For each box in $x_1 x_2 x_3 x_4$-space, two points $(x_1, x_2, x_3, x_4)_I$ and $(x_1, x_2, x_3, x_4)_{II}$ are chosen pseudo-randomly. The bulk of the evaluation of $L_{\sigma\sigma}$ and $p_\sigma L_{\sigma\tau} p_\tau$, which consists of several thousand operations, is carried out at this level of the integration. This is possible because the relatively simple dependence upon ϕ_{3B} and ϕ_{1A} can be factored out.

At each of the points chosen above all expressions independent of ϕ_{3B} and ϕ_{1A} are computed. N_5 pseudo-random values of ϕ_{3B} are then selected (one in each of the ϕ_{3B} intervals). For each ϕ_{3B} value, $k\cdot k_2$, $k_1\cdot k_2$, $k\cdot k$, and $k_1\cdot k_3$ are calculated (see Appendix A), and all expressions independent of ϕ_{1A} are computed. Finally, N_6 pseudo-random values of ϕ_{1A} (one per interval) are selected, the integrand is computed at each ϕ_{1A} value, and the values of q^2 and (in the lab frame) of kinetic energy T_i, $\log_{10}(1 - \cos\theta_i)$ where θ_i is the angle made with the forward direction, the transverse momentum $k_{\perp i} = |\vec{k}| \sin\theta_i$, and the quantity $\Delta k_{\parallel i} = |\vec{k}|(1 - \cos\theta_i)$, each for i = 1, 2, 3, are computed. (See Appendix A for details of the T_i and $\cos\theta_i$ computations.) The differential cross section for each point (i.e., each simulated "event") is assigned to the appropriate one of a large number (≥ 10000) of internally-carried bins in each of

these variables. At the end of the calculations histograms are generated in these variables. Each histogram contains about 25 bins, which are selected so that an approximately equal partial cross section $\Delta\left(\frac{d\sigma}{dv}\right)$ falls within each bin.

Because the vast majority of the integrand calculations are done inside only four of the six integrations, the bulk of the computing time is spent in the calculation of the bin assignments rather than of the integrand. For given values of v and incoming muon energy E, the calculation of $\frac{d\sigma}{dv}$ and its distribution in q^2 and in the laboratory variables given above, requires about a minute of computing on an IBM 360/95.

Since each set of $x_{1\to4}$ values is selected independently and pseudo-randomly, a statistically unbiased estimate of the accuracy of the $x_{1\to4}$ integrations is given by the variance

$$(\text{s.d.})^2 = (2N_1N_2N_3N_4)^{-2} \Sigma \left[f(x_{1\to4})_I - f(x_{1\to4})_{II}\right]^2 \qquad (4.5)$$

summed over all points in $x_1x_2x_3x_4$-space, where f is the integrand of the $x_{1\to4}$ integrations (already integrated over ϕ_{3B} and ϕ_{1A}) and "s.d." denotes the standard deviation. The total integral is given by the approximation

$$\frac{d\sigma}{dv} = (2N_1N_2N_3N_4)^{-1} \Sigma \left[f(x_{1\to4})_I + f(x_{1\to4})_{II}\right] . \qquad (4.6)$$

For the results presented, (s.d.)/($d\sigma$/dv) is approximately 2% or less.

The reproducibility of the values of $d\sigma/dv$ and of the kinematic distributions (i.e., for different sets of pseudo-random numbers) has been tested for several cases; the $d\sigma/dv$ values given are reproducible to within about 2%, and each of the approximately 25 bin populations (for each distribution) to within 10%. An independent estimate of the accuracy of some of the kinematic distributions is obtained by noting the extent of the discrepancies between the e^+ and e^- distributions, which by symmetry would be identical in an exact calculation. The differences in the e^+ and e^- bin populations are found to be on the order of several percent.

V. VIRTUAL COMPTON GRAPHS

Rather than considering in detail the complexities of the hadronic interaction in the two-photon-exchange case [Fig. 2(a)], we have calculated the contribution of the virtual Compton graphs for scattering off protons, according to a simple model.[10] In this model, the proton is treated as though it were bare, except that an overall dipole form factor $G[(p'-p)^2]$ [see Eq. (2.7)] is incorporated into the matrix element. Apart from the factor G, the two virtual Compton graphs are then given in Figs. 2(b) and (c). Under the substitutions[11]

$$\begin{aligned} m_u &\longmapsto M \\ k &\longmapsto p \\ k_1 &\longmapsto p' \end{aligned} \tag{5.1}$$

these diagrams become identical to graphs (a) and (b) of Fig. 1 (for Z = bare proton). This circumstance makes it possible to calculate the singly-differential cross section for virtual Compton scattering by the same method as that used in Sections II and III (and the Appendices), if one replaces K_σ by T_σ in Eq. (2.1), makes the substitutions (5.1), and includes the appropriate form factor. The transformation of Section IV is replaced by a more appropriate one:

$$\begin{aligned} x_1 &= \ln t \\ x_2 &= u_1 \\ x_3 &= \int_{u_2}^{\infty} G\,(u_2' - \nu - t)^2\, du_2' \\ x_4 &= u_3 \end{aligned} \tag{5.2}$$

where t and u_i (i = 1, 2, 3) are defined as in Eq. (3.2) with the substitutions (5.1) applied [thus $t = (k_1-k)^2$, etc.]. The virtual Compton graphs will be found (see Section VI) to make a negligible contribution to the cross section for the large ν values of interest.

VI. RESULTS AND DISCUSSION

We have calculated $(d\sigma/dv)$ and its distributions in q^2 and the lab quantities T_i, $\cos\theta_i$, $k_{\perp i}$, and $\Delta k_{\parallel i}$, for several types of cross sections σ of interest. σ_p and σ_{Fe} denote the cross sections for the Bethe-Heitler process [Fig. 1(a)-(d)] for elastic scattering off a free proton and coherent scattering off iron, respectively. The cross sections corresponding to the two Bethe-Heitler graphs which contain a timelike photon of mass $\sqrt{v}$ [i.e., graphs (a) and (b) of Fig. 1, which are calculated by replacing K_σ by T_σ in Eq. (2.1)] are denoted by σ_p' and σ_{Fe}'. The cross section for virtual Compton scattering off a free proton (calculated according to graphs (b) and (c) of Fig. 2, with the dipole form factor $G[(p'-p)^2]$ included in the matrix element) is denoted by σ_p''.

In Fig. 3, $d\sigma_p/dv$ and $d\sigma_p'/dv$ are plotted versus v, the (e^-e^+) mass squared, for incident muon energies of 200 and 300 GeV.

As discussed in the Introduction, we are interested in the use of kinematic cuts to increase the ratio $\left(\frac{d\sigma_p'}{dv}\right)\Big/\left(\frac{d\sigma_p}{dv}\right)$ (and similarly for Z = Fe). It is efficient for these purposes to make such a cut in $\cos\theta_{1,\,lab}$, where $\theta_{1,\,lab}$ is the lab angle of the outgoing muon relative to the incoming beam. For reasons to be discussed below, the somewhat arbitrary cut $\cos\theta_{1,\,lab} \leq 0.996$ has been chosen for further study. We define $\sigma_{p,c}$ as that portion of σ_p which arises from all kinematic configurations satisfying $\cos\theta_{1,\,lab} \leq 0.996$; $\sigma_{p,c}'$, $\sigma_{Fe,c}'$, and $\sigma_{Fe,c}'$ are defined *mutatis mutandis*.

For electron pair masses of $\sqrt{v}$ = 5, 10, and 15 GeV and incoming muon energy E = 100, 200, and 300 GeV, Table I gives $(1/Z)(d\sigma/dv)$ where σ denotes the five types of cross sections σ_p, σ_{Fe}, σ_p', σ_{Fe}', and σ_p''. The average values of q^2 and the lab quantities T_1, $T_{2,3}$, $\cos\theta_1$, $\cos\theta_{2,3}$, $k_{\perp 1}$, $k_{\perp 2,3}$, $\Delta k_{\parallel 1}$, and $\Delta k_{\parallel 2,3}$ are also given. (The subscript "2,3" indicates that the electron and positron distributions have been averaged together; this is reasonable since these distributions would be identical in an exact calculation.) For three of the $(\sqrt{v}, E)$ pairs, Table I also gives $(1/Z)(d\sigma/dv)$ and the average values of the kinematic quantities for the case of $\sigma_{p,c}$, $\sigma_{p,c}'$, $\sigma_{Fe,c}$, and $\sigma_{Fe,c}'$.

For the case $\sqrt{v}$ = 10 GeV, E = 300 GeV, Fig. 4 gives (in histogram form) the computed distributions in T_1 and $T_{2,3}$ for each of the singly-differential cross sections $d\sigma_p/dv$, $d\sigma_p'/dv$, $d\sigma_{p,c}/dv$, and $d\sigma_{p,c}'/dv$. Figure 5 gives the corresponding distributions in $\log_{10}(1-\cos\theta_1)$ and $\log_{10}(1-\cos\theta_{2,3})$; Fig. 6, in $\Delta k_{\perp 1}$ and $\Delta k_{\perp 2,3}$; and Fig. 7, in q^2.

We list several results of the calculations below.

1. For the $(\sqrt{v}, E)$ values of Table I, $d\sigma_p/dv$ is at least an order of magnitude greater than $(1/26)(d\sigma_{Fe}/dv)$ [and likewise $d\sigma_p'/dv \gg (1/26)(d\sigma_{Fe}'/dv)$] except far from threshold (at $\sqrt{v}$ = 5 GeV, E ≥ 200 Gev).

2. An essential check on the calculation of $d\sigma'/dv$ for Z = p and Fe is obtained by comparing $d\sigma'/dv$ with the total cross section $\sigma(B^0)$ for production of B^0 bosons of mass $\sqrt{v}$ via process (1.4). By comparing

the results of Sections II and III with the cross section formulae of paper I, one finds

$$\sigma(B^0) = (3\pi v/\alpha)(1 + 2m_e^2/v)^{-1}\,(1 - 4m_e^2/v)^{-1/2}\,(d\sigma'/dv)\ . \qquad (5.1)$$

The numerical results for $d\sigma'/dv$ satisfy Eq. (5.1) to within approximately 2%.

3. In general, $d\sigma_p/dv \cong 100(d\sigma'_p/dv) \gtrsim 10^4(d\sigma''_p/dv)$. This can be roughly understood in terms of the propagator denominators. In $d\sigma_p/dv$, the "spacelike" term S [Eq. (2.4)], with its overall factor of $D = (k - k_1)^2$ in the denominator, dominates the matrix element; while the matrix element for $d\sigma'_p/dv$ contains the denominator v instead. Ignoring muon mass terms, $D \cong 2E\Delta k_{\parallel 1}$, which typically is several GeV^2 for $d\sigma_p/dv$ (see Table I). Therefore one would crudely expect that $(d\sigma_p/dv)/(d\sigma'_p/dv) \cong O(v^2/D^2) \cong O(10^3)$; in reality the ratio of cross sections is closer to 100.

To see why the virtual Compton cross section $d\sigma''_p/dv$ is so small, we consider the factors arising from the photon propagators and the hadronic form factor $G(q^2)$. For $d\sigma'_p/dv$ these factors give $v^{-2}q^{-4}G^2(q^2)$; for $d\sigma''_p/dv$ they give $v^{-2}D^{-2}G^2(q^2)$. Using the average values of these quantities (obtained from Table I), one finds $(d\sigma'_p/dv)/(d\sigma''_p/dv) \cong O(100)$.

4. For the case of $d\sigma_p/dv$ and $d\sigma_{Fe}/dv$, the outgoing muon typically comes out nearly forward and has a moderately flat energy spectrum; while the electron and positron come out at large angles from the forward direction and have spectra which are strongly peaked at small energies. (See Figs. 4 and 5.) The value of $\langle T_{2,3}\rangle_{av}$ is somewhat misleading in this respect, because of the highly skewed distribution. Although (for $d\sigma_p/dv$ with $\sqrt{v}$ = 10 GeV, E = 300 GeV) the mean $T_{2,3}$ is 99 GeV and the median is ≅ 85 GeV, 40% of the $T_{2,3}$ distribution falls below 15 GeV. A similar situation occurs for other ($\sqrt{v}$, E) values.

5. By way of contrast, $d\sigma'_p/dv$ (and $d\sigma'_{Fe}/dv$) exhibit distributions very different from those above. The outgoing muon is on the average slow and comes out at a large angle (≅ 20°); while the electron and positron are fast, have moderately flat spectra, and come out at a somewhat smaller angle (≅ 5°). This is the situation which would occur in the case of resonant electron pair production via process (1.4).

6. Because there is such a slight overlap between the $\log_{10}(1 - \cos\theta_1)$ distributions of $d\sigma_p/dv$ and $d\sigma'_p/dv$ [see Fig. 5(a)], one can choose a cutoff value of $\cos\theta_1$, called c', such that ≥98% of $d\sigma_p/dv$ lies above c', and ≥50% of $d\sigma'_p/dv$ lies below c'. A suitable (though not unique) choice, based upon Fig. 5(a) and similar distributions at other ($\sqrt{v}$, E) values, is c' = 0.996 (for which $\log_{10}(1 - c') \cong -2.4$). For this cutoff, inspection of Figs. 4 - 7 indicates that the $d\sigma_{p,c}/dv$ distributions are generally similar to those of $d\sigma'_p/dv$, while retaining some of the $d\sigma_p/dv$ peaks that arise from propagator denominators.

Because of the large qualitative differences between the $d\sigma_p/dv$ and $d\sigma_p'/dv$ distributions, we conclude that it is possible, by imposing the appropriate kinematic cuts suggested by Figs. 4 - 7, to design experiments which are highly sensitive to possible modifications in the timelike-photon Bethe-Heitler graphs at large values of v, the $(e^- e^+)$ mass squared. The competing contribution of the spacelike-photon graphs can be made comparable to the timelike contribution, while the virtual Compton cross section is extremely small, according to the simple model used here. Although a cut in $\cos\theta_L$ has been considered for purposes of illustration, favorable results can be achieved by making cuts in other variables as well.

ACKNOWLEDGEMENTS

I am grateful to Professor T. D. Lee for suggesting this problem, and for essential advice and encouragement throughout the course of the work. The problem originally arose as a result of suggestions by Professor L. M. Lederman concerning muon trident experiments. I have profited also from discussions with Professors N. H. Christ, Wonyong Lee, and Luke Mo, with Drs. R. W. Brown and Jack Smith, and with Mr. Allan Rothenberg.

APPENDIX A

Using the definitions of Eqs. (2.5), (3.2) ff., and (3.5), the dot products of k, k_1, k_2, k_3, q, and p are calculated as follows. We have

$$k\cdot k_1 = \frac{1}{2}\left(v + t - u_2\right) - m_u^2$$

$$k\cdot q = u_1$$

$$k\cdot p = - Mk_{0,lab}$$

$$k_1\cdot q = u_1 - \frac{1}{2}u_2$$

$$k_2\cdot k_3 = m_e^2 - \frac{1}{2}v$$

$$k_2\cdot q = -\frac{1}{2}t + \frac{1}{4}u_2 + \frac{1}{2}u_3$$

$$k_3\cdot q = -\frac{1}{2}t + \frac{1}{4}u_2 - \frac{1}{2}u_3$$

$$q\cdot p = -\frac{1}{2}t \quad . \tag{A.1}$$

In frame "B" the polar and azimuthal coordinates are denoted θ_B and ϕ_B; the z axis is defined to lie along the $\theta_B = 0$ ray, and the x and y axes satisfy $(\theta_B, \phi_B) = (\frac{\pi}{2}, 0)$ and $(\frac{\pi}{2}, \frac{\pi}{2})$, respectively. By definition, $k_{yB} = q_{xB} = q_{yB} = 0$, and we define the sense of ϕ_B such that $p_{yB} \geq 0$. Thus

$$k\cdot k_3 = k_{xB}k_{3xB} + k_{zB}k_{3zB} - k_{0B}k_{30B} \quad . \tag{A.2}$$

We have

$$q_{0B} = \frac{1}{\sqrt{v}}\left(t - \frac{1}{2}u_2\right)$$

$$|\vec{q}|_B = \frac{1}{2}\sqrt{\frac{\delta}{v}}$$

$$k_{0B} = \frac{\eta}{2\sqrt{v}} \tag{A.3}$$

where

$$\eta = v + t - u_2 + 2u_1 \quad ; \tag{A.4}$$

thus

$$k_{zB} = \left(u_1 + k_{0B}q_{0B}\right)/|\vec{q}|_B$$

and

$$k_{xB} = \left(k_{0B}^2 - k_{zB}^2 - m_u^2\right)^{1/2} \tag{A.5}$$

can be calculated. Using

$$k_{30B} = \frac{1}{2}\sqrt{v}$$

and

$$k_{3zB} = -u_3\sqrt{\frac{v}{\delta}} \quad , \tag{A.6}$$

one obtains

$$k_{3\left\{\begin{matrix}x\\y\end{matrix}\right\}B} = \left(\frac{1}{4}v - m_e^2 - \frac{u_3^2 v}{\delta}\right)^{1/2} \left\{\begin{matrix}\cos\\\sin\end{matrix}\right\}\phi_{3B} \quad . \tag{A.7}$$

Therefore

$$k\cdot k_3 = -\frac{1}{4}\eta - \frac{u_3\zeta}{\delta} + \left[\left(\frac{1}{4}\eta^2 - m_\mu^2 v - \frac{\zeta^2}{\delta}\right)\left(\frac{1}{4} - \frac{m_e^2}{v} - \frac{u_3^2}{\delta}\right)\right]^{1/2}\cos\phi_{3B} \qquad (A.8)$$

where

$$\zeta = 2vu_1 + \eta\left(t - \frac{1}{2}u_2\right) . \qquad (A.9)$$

The other dot products that depend upon ϕ_{3B} but not upon ϕ_{1A}, are

$$k\cdot k_2 = -\frac{1}{2}\eta - k\cdot k_3 ,$$

$$k_1\cdot k_2 = -u_1 + \frac{1}{4}u_2 - \frac{1}{2}u_3 - k\cdot k_3$$

and

$$k_1\cdot k_3 = \frac{1}{2}\left(v + t + u_3\right) - \frac{1}{4}u_2 + k\cdot k_3 . \qquad (A.10)$$

In frame "A" the angular coordinates are denoted θ_A and ϕ_A; the x, y, and z axes for frame "A" are defined in terms of θ_A and ϕ_A as described above (for frame "B"). By definition, $p_{yA} = k_{xA} = k_{yA} = 0$, and the sense of ϕ_A is arbitrary. We have

$$k_1\cdot p = k_{1xA}\,p_{xA} + k_{1zA}\,p_{zA} - k_{10A}\,p_{0A} \qquad (A.11)$$

where

$$k_{10A} = \left(u_1 + m_\mu^2 - \frac{1}{2}v - \frac{1}{2}t\right)/\sqrt{\beta}$$

$$k_{1zA} = \frac{\left[\left(u_1 - t\right)\left(v - m_\mu^2\right) + \beta\left(t + u_1 - u_2\right)\right]}{2(\beta\epsilon)^{1/2}}$$

$$k_{1xA} = \left[\frac{\left(u_1 - \frac{1}{2}v - \frac{1}{2}t\right)^2 - m_\mu^2 v}{\beta} - k_{1zA}^2\right]\cos\phi_{1A}$$

$$p_{0A} = \left(Mk_{0,lab} - \frac{1}{2}t\right)/\sqrt{\beta}$$

$$p_{zA} = \left[Mk_{0,lab}\left(t - u_1\right) - \frac{1}{2}t\left(u_1 + m_\mu^2\right)\right]\Big/(\beta\epsilon)^{\frac{1}{2}}$$

$$p_{xA} = \left[\frac{\left(M^2 k_{0,lab}^2\, t - Mk_{0,lab}\, tu_1 - \frac{1}{4}m_\mu^2 t^2\right)}{\epsilon} - M^2\right]^{1/2} \qquad (A.12)$$

with

$$\beta = 2u_1 + m_\mu^2 - t$$

and

$$\epsilon = u_1^2 + m_\mu^2 t . \qquad (A.13)$$

Also

$$k_3\cdot p = k_{3xB}\,p_{xB} + k_{3yB}\,p_{yB} + k_{3zB}\,p_{zB} - k_{30B}\,p_{0B}$$

where

$$p_{0B} = \left(M k_{0,lab} - \frac{1}{2} t + k_1 \cdot p\right) / \sqrt{v}$$

$$p_{zB} = \left[\left(2t - u_2\right) p_{0B} - t\sqrt{v}\right] / \sqrt{b}$$

$$p_{xB} = \left(k_{0B} p_{0B} - M k_{0,lab} - k_{zB} p_{zB}\right) / k_{xB}$$

$$p_{yB} = \left(p_{0B}^2 - M^2 - p_{xB}^2 - p_{xB}^2\right)^{1/2} \qquad \text{(A. 14)}$$

nd $k_{3\lambda B}$, $k_{\lambda B}$ are given by Eqs. (A. 3) through (A. 7), for $\lambda = 0, x, y, z$.

The propagator denominators are therefore [see Eq. (2. 5)]

$$D = u_2 - y - t$$

$$D_a = t - 2u_1$$

$$D_b = t + 2u_1 - u_2$$

$$D_c = \frac{1}{2} u_2 + u_3$$

$$D_d = \frac{1}{2} u_2 - u_3 \quad . \qquad \text{(A. 15)}$$

Using these results, it is straightforward to derive expressions for the b variables over which the kinematic distributions are obtained. The netic energies of the outgoing leptons are

$$T_i = E_i - m_i \qquad (i = 1, 2, 3)$$

where $m_1 = m_\mu$, $m_2 = m_3 = m_e$, and

$$E_i = - k_i \cdot p / M \qquad (i = 1, 2, 3) \quad . \qquad \text{(A. 16)}$$

Also

$$\cos\theta_i = \frac{\mathbf{k} \cdot \mathbf{k}_i + E E_i}{|\mathbf{k}|_{lab} |\mathbf{k}_i|_{lab}} \qquad (i = 1, 2, 3) \qquad \text{(A. 17)}$$

where $E = k_{0,lab}$ and $|\mathbf{k}_i|_{lab} = \left(E_i^2 - m_i^2\right)^{1/2}$.

APPENDIX B

The integration domains for the azimuthal angles ϕ_p, ϕ_{3B}, and ϕ_{1A}, each extend from 0 to 2π. The ϕ_p integration is trivial. Since all computed quantities are invariant under the mapping $\phi_1 \to 2\pi - \phi_1$, it is convenient to integrate over ϕ_{1A} from 0 to π only, and multiply by two.[7]

The limits of the u_3 integration arise from the condition

$$|\cos\theta_{3B}| \leq 1 \tag{B.1}$$

where $\theta_{3B} = \angle(\vec{q}, \vec{k}_3)$ in frame "B" (in which frame $\vec{k} - \vec{k}_1 = \vec{q}$). One obtains

$$u_{3-} \leq u_3 \leq u_{3+}$$

where [see Eq. (3.5)]

$$u_{3+} = -u_{3-} = \left[\left(\frac{1}{4} - \frac{m_e^2}{v}\right)\delta\right]^{1/2} . \tag{B.2}$$

Similarly, one requires

$$|\cos\theta_{1A}| \leq 1 \tag{B.3}$$

where $\theta_{1A} = \angle(\vec{q}, \vec{k}_1)$ in frame "A" (in which frame $\vec{k} = \vec{q}$). Therefore

$$u_{2-} \leq u_2 \leq u_{2+}$$

where [see Eqs. (A.13)]

$$u_{2\pm} = t + u_1 + \left\{(v - m_u^2)(u_1 - t) \pm \left[(2u_1 - v - t)^2 - 4m_u^2 v\right]^{1/2} \sqrt{t}\right\} / 3 . \tag{B.4}$$

The domain of u_1 is given by

$$u_{1-} \leq u_1 \leq u_{1+}$$

where u_{1-} is the value at which the physical u_2 region vanishes,

$$u_{1-} = \frac{1}{2}v + \frac{1}{2}t + m_u\sqrt{v} . \tag{B.5}$$

and where u_{1+} corresponds to the nucleon or nucleus coming out forward in the lab frame,

$$u_{1+} = |\vec{k}|_{lab}\left[t + (t/2M)^2\right]^{1/2} - k_{0,lab}\, t/2M . \tag{B.6}$$

Requiring $u_{1-} \leq u_{1+}$ yields the kinematic limits on t:

$$t_- \leq t \leq t_+$$

where $t_\pm$ are the roots of

$$at^2 + bt + c = 0 \tag{B.7}$$

with

$$a = \frac{1}{4} + \frac{k_{0,lab}}{2M} + \frac{m_u^2}{4M^2}$$

$$b = \left(\frac{k_{0,lab}}{M} + 1\right)\left(\frac{1}{2}v + m_u\sqrt{v}\right) - |\vec{k}|_{lab}^2$$

$$c = \left(\frac{1}{2}v + m_u\sqrt{v}\right)^2 . \tag{B.8}$$

The limits on u_2, u_1, and t are similar to the corresponding limits in B^0 production (Paper I), since the mass ($\sqrt{v}$) of the virtual timelike photon [in diagrams (a) and (b) of Fig. 1] is fixed. This renders the kinematics similar to that for the case of three outgoing particles (nucleon or nucleus, lepton, and virtual photon), if one is not specifically interested in the $\vec{k}_2$ and $\vec{k}_3$ distributions.

The threshold beam energy for given v is

$$\left(k_{0,\,lab}\right)_{\cdot} = \frac{1}{M}\left(\frac{1}{2}v + m_u\sqrt{v}\right) + m_u + \sqrt{v} \quad . \tag{B. 9}$$

It is sometimes useful (see Section VI) to be able to integrate over only that portion of kinematically available phase space which satisfies an arbitrary constraint such as

$$\cos\theta_{1,\,lab} \leq c' \quad . \tag{B. 10}$$

An efficient means of doing this, which avoids calculating the integrand where it is unnecessary, is given below for the particular constraint (B. 10). Cuts in other variables can be treated similarly.

Equations (A. 11) – (A. 13) and (A. 16) – (A. 17) imply that $\cos\theta_{1,\,lab}$ is of the form

$$\cos\theta_{1,\,lab} = \frac{c_1 + c_2\cos\phi_{1A}}{\left(c_3 + c_4\cos\phi_{1A} + c_5\cos^2\phi_{1A}\right)^{1/2}} \tag{B. 11}$$

where the c_i ($i = 1, \ldots, 5$) are independent of ϕ_{1A} and ϕ_{3B}. Therefore

$$\frac{\partial\left(\cos\theta_{1,\,lab}\right)}{\partial\left(\cos\phi_{1A}\right)} = 0 \tag{B. 12}$$

if and only if

$$\cos\phi_{1A} = \frac{c_1 c_4 - 2c_2 c_3}{c_2 c_4 - 2c_1 c_5} \tag{B. 13}$$

For each choice of t, u_1, u_2, and u_3, the values of $\cos\theta_{1,\,lab}$ obtained by setting $\cos\phi_{1A}$ equal to +1, -1, and the RHS of Eq. (B. 13) [if the absolute value of (B. 13) is < 1] are each calculated using (B. 11). If each of the resulting values of $\cos\theta_{1,\,lab}$ exceeds the cutoff c′ of (B. 10), then no possible ϕ_{1A} can satisfy (B. 10), and the entire phase space region corresponding to the given values of t and u_{1-3} must fall outside the cut. If, on the other hand, some ϕ_{1A} satisfies (B. 10), then the calculation of $L_{\sigma\sigma}$ and $p_\sigma L_{\sigma\tau} p_\tau$ proceeds as usual, and each pseudo-randomly selected ϕ_{1A} is tested separately for the criterion (B. 10).

FOOTNOTES

[1] T. D. Lee, in *Topical Conference on Weak Interactions, CERN, Geneva, Switzerland, 14-17 January 1969* (CERN Scientific Information Service, Geneva, Switzerland, 1969), p. 427.

[2] T. D. Lee and G. C. Wick, Phys. Rev. D 2, 1033 (1970).

[3] R. Linsker, Phys. Rev. Lett. 27, 167 (1971).

[4] R. Linsker, to be published. (Hereafter called I.)

[5] Throughout the paper, $\hbar = c = 1$ and $e^2 = 4\pi\alpha$, where $\alpha \cong 1/137$. The metric used is such that $a \cdot b = \vec{a} \cdot \vec{b} + a_4 b_4$, $a_4 = ia_o$. All γ matrices are Hermitian.

[6] D. H. Coward et al, Phys. Rev. Lett. 20, 292 (1968); W. K. H. Panofsky, in *Proceedings of the Fourteenth International Conference on High-Energy Physics, Vienna, Austria, September, 1968*, edited by J. Prentki and J. Steinberger (CERN Scientific Information Service, Geneva, Switzerland, 1968), p. 23.

[7] See for example J. Lovseth and M. Radomski, Phys. Rev. D 3, 2686 (1971).

[8] R. W. Brown and J. Smith, Phys. Rev. D 3, 207 (1971).

[9] M. Veltman, unpublished.

[10] This simple model was suggested by T. D. Lee on the basis of scaling arguments; the model is intended to be used only at the large (e^*) masses considered here.

[11] The formal substitutions (5.1) are used only to simplify the description of the virtual Compton cross section computations. In Section VI, all variables revert to their original meanings; thus, for example, q in Section VI denotes the hadronic momentum transfer $(p' - p)$, and not the muon momentum transfer $(k_1 - k)$ [which q would have represented under the substitutions (5.1)].

TABLE CAPTION

Table I. Singly-differential cross section per proton $(1/Z)(d\sigma/dv)$ and average values of kinematic quantities, for process (1.1) with Z = p and Z = Fe. [The quantity v denotes the $(e^- e^+)$ pair mass squared.] Several types of cross sections σ are considered: σ_p and σ_{Fe} are calculated using the four Bethe-Heitler graphs of Fig. 1; σ'_p and σ'_{Fe} refer to the two "timelike" Bethe-Heitler graphs only [Fig. 1(a) and (b)]; $\sigma_{p,c}$, $\sigma_{Fe,c}$, $\sigma'_{p,c}$, and $\sigma'_{Fe,c}$ are the corresponding cross sections with the cut $\cos\theta_1 \leq 0.996$ imposed. σ''_p denotes the virtual Compton cross section (Fig. 2).

FIGURE CAPTIONS

Fig. 1. Bethe-Heitler graphs for process (1.1). The virtual photon carrying momentum q can be attached at any of positions (a) - (d). In diagrams (a) and (b), the unlabeled virtual photon is timelike; in (c) and (d), it is spacelike.

Fig. 2. Virtual Compton graph for process (1.1). (a) General structure. (b) and (c) Graphs under the assumption that Z = bare proton.

Fig. 3. Distribution in $(e^- e^+)$ mass squared, v, for process (1.1) with Z = p and E = 200 and 300 GeV, for the four Bethe-Heitler (BH) graphs (——) and for the two "timelike" BH graphs alone (- - -).

Fig. 4. Normalized kinematic distributions in lab kinetic energy for process (1.1) with Z = p, $\sqrt{v}$ = 10 GeV, and E = 300 GeV, for the four Bethe-Heitler (BH) graphs(——) and for the two "timelike" BH graphs alone (· · · ·). [The quantity v denotes the $(e^- e^+)$ pair mass squared.] (a) T_1 distribution with no kinematic cut imposed; (b) T_1, with the cut $\cos\theta_1 \leq 0.996$; (c) $T_{2,3}$, no cut; (d) $T_{2,3}$, with same cut.

Fig. 5. Same as Fig. 4, but for distributions in the lab-frame variables $\log_{10}(1 - \cos\theta_1)$ and $\log_{10}(1 - \cos\theta_{2,3})$.

Fig. 6. Same as Fig. 4, but for distributions in the lab transverse momenta $k_{\perp 1}$ and $k_{\perp 2,3}$.

Fig. 7. Same as Fig. 4, but for distributions in q^2.

TABLE I

$\sqrt{\nu}$ (GeV)	E (GeV)	Type of σ	$\frac{1}{Z}\frac{d\sigma}{d\nu}$ $\left(10^{-38}\frac{cm^2}{GeV^2}\right)$	T_1 (GeV)	$T_{2,3}$ (GeV)	$\cos\theta_1$	$\cos\theta_{2,3}$	$k_{\perp 1}$ (GeV)	$k_{\perp 2,3}$ (GeV)	$\Delta k_{\parallel 1}$ (GeV)	$\Delta k_{\parallel 2,3}$ (GeV)	q^2 (GeV^2)
5	100	σ_p	3.85	39.1	30.3	0.9985	0.769	0.38	0.89	0.0058	0.120	0.322
		σ_{Fe}	0.0686	18.0	41.0	0.9986	0.702	0.26	0.72	0.0046	0.079	0.051
		σ'_p	0.0576	8.1	45.8	0.9304	0.987	0.64	1.90	0.0573	0.072	0.246
		σ'_{Fe}	0.00180	3.8	48.1	0.9558	0.989	0.27	1.85	0.0203	0.066	0.048
		σ''_p	0.000270	60.6	19.4	0.9996	0.941	0.58	1.92	0.0083	0.195	0.899
5	200	σ_p	14.1	100.7	49.6	0.9994	0.819	0.41	0.84	0.0031	0.083	0.225
		σ_{Fe}	6.00	43.9	78.0	0.9996	0.761	0.30	0.68	0.0025	0.042	0.016
		σ'_p	0.159	17.0	91.4	0.9549	0.996	0.76	1.93	0.0443	0.038	0.160
		σ'_{Fe}	0.130	9.1	95.4	0.9904	0.996	0.32	1.86	0.0115	0.033	0.014
		σ''_p	0.000422	155.4	22.0	0.9999	0.935	0.61	1.92	0.0044	0.186	0.869
		$\sigma_{p,c}$	0.112	4.2	97.8	0.9327	0.971	0.61	1.64	0.0623	0.033	0.161
		$\sigma_{Fe,c}$	0.0741	2.0	98.9	0.9798	0.900	0.27	1.38	0.0201	0.032	0.016
		$\sigma'_{p,c}$	0.0793	3.3	98.2	0.9096	0.997	0.55	1.90	0.0675	0.033	0.168
		$\sigma'_{Fe,c}$	0.0454	1.4	99.2	0.9731	0.997	0.22	1.86	0.0193	0.032	0.016
5	300	σ_p	25.4	168.5	65.6	0.9996	0.839	0.43	0.83	0.0021	0.069	0.189
		σ_{Fe}	28.5	86.1	106.9	0.9998	0.799	0.35	0.68	0.0019	0.032	0.011
		σ'_p	0.234	26.4	136.7	0.9663	0.998	0.83	1.94	0.0373	0.026	0.133
		σ'_{Fe}	0.506	15.8	142.1	0.9927	0.998	0.39	1.87	0.0107	0.023	0.010
		σ''_p	0.000496	252.6	23.4	1.0000	0.940	0.62	1.95	0.0030	0.181	0.820
10	100[a]	σ_p	0.00152	11.2	43.9	0.9974	0.681	0.29	1.68	0.0088	0.289	1.512
		σ'_p	2.04×10^{-5}	4.7	47.2	0.9707	0.963	0.50	3.67	0.0128	0.267	1.397
		σ''_p	3.83×10^{-7}	15.4	41.6	0.9972	0.957	0.39	3.70	0.0117	0.307	2.376
10	200	σ_p	0.0669	51.4	74.1	0.9988	0.737	0.47	1.51	0.0069	0.178	0.562
		σ_{Fe}	5.91×10^{-5}	23.1	88.4	0.9983	0.664	0.32	1.31	0.0057	0.144	0.128
		σ'_p	0.000996	11.4	94.1	0.9520	0.988	0.82	3.73	0.0611	0.136	0.464
		σ'_{Fe}	1.55×10^{-6}	4.7	97.6	0.9645	0.989	0.34	3.69	0.0259	0.129	0.120
		σ''_p	2.68×10^{-6}	77.6	60.8	0.9995	0.971	0.73	3.74	0.0105	0.226	1.250
		$\sigma_{p,c}$	0.00180	6.1	96.8	0.9629	0.898	0.81	2.56	0.0667	0.131	0.453
		$\sigma_{Fe,c}$	3.08×10^{-6}	3.3	98.3	0.9676	0.736	0.43	2.01	0.0337	0.128	0.122
		$\sigma'_{p,c}$	0.000622	4.2	97.7	0.9175	0.989	0.70	3.71	0.0820	0.129	0.464
		$\sigma'_{Fe,c}$	9.71×10^{-7}	1.8	99.1	0.9234	0.989	0.30	3.66	0.0373	0.127	0.124

10	300	σ_p	0.215	101.6	99.0	0.9991	0.774	0.55	1.46	0.0054	0.140	0.407
		σ_{Fe}	0.00125	54.1	122.9	0.9988	0.726	0.42	1.30	0.0049	0.104	0.083
		σ'_p	0.00285	18.4	140.7	0.9460	0.994	0.96	3.76	0.0596	0.092	0.318
		σ'_{Fe}	2.73×10^{-5}	9.8	145.1	0.9534	0.994	0.49	3.71	0.0300	0.087	0.080
		σ''_p	4.32×10^{-6}	158.9	70.2	0.9998	0.979	0.88	3.77	0.0082	0.206	1.043
		$\sigma_{p,c}$	0.00290	5.8	147.0	0.9420	0.937	0.80	2.87	0.0737	0.086	0.314
		$\sigma_{Fe,c}$	2.93×10^{-5}	3.3	148.3	0.9515	0.878	0.45	2.58	0.0395	0.085	0.080
		$\sigma'_{p,c}$	0.00159	4.2	147.8	0.9068	0.994	0.70	3.73	0.0835	0.086	0.319
		$\sigma'_{Fe,c}$	1.54×10^{-5}	2.0	149.0	0.9197	0.994	0.34	3.69	0.0409	0.084	0.081
15	200[a]	σ_p	0.000146	18.4	90.2	0.9984	0.688	0.33	2.23	0.0075	0.315	2.008
		σ'_p	1.87×10^{-6}	7.4	95.8	0.9827	0.978	0.59	5.53	0.0388	0.295	1.831
		σ''_p	2.20×10^{-8}	25.3	86.5	0.9985	0.971	0.45	5.54	0.0098	0.330	3.046
15	300	σ_p	0.00332	51.5	124.0	0.9990	0.721	0.49	2.11	0.0072	0.232	0.910
		σ_{Fe}	2.43×10^{-7}	18.9	140.5	0.9981	0.634	0.29	1.88	0.0055	0.201	0.203
		σ'_p	4.92×10^{-5}	13.0	143.2	0.9737	0.989	0.88	5.58	0.0557	0.199	0.790
		σ'_{Fe}	6.81×10^{-9}	4.3	147.8	0.9595	0.989	0.31	5.53	0.0227	0.191	0.202
		σ''_p	1.21×10^{-7}	75.1	122.0	0.9994	0.982	0.73	5.58	0.0104	0.262	1.616

[a] For these $\sqrt{\nu}$ and E, the calculated σ_{Fe} and σ'_{Fe} are zero because of the cutoff factor in Eq. (2.12).

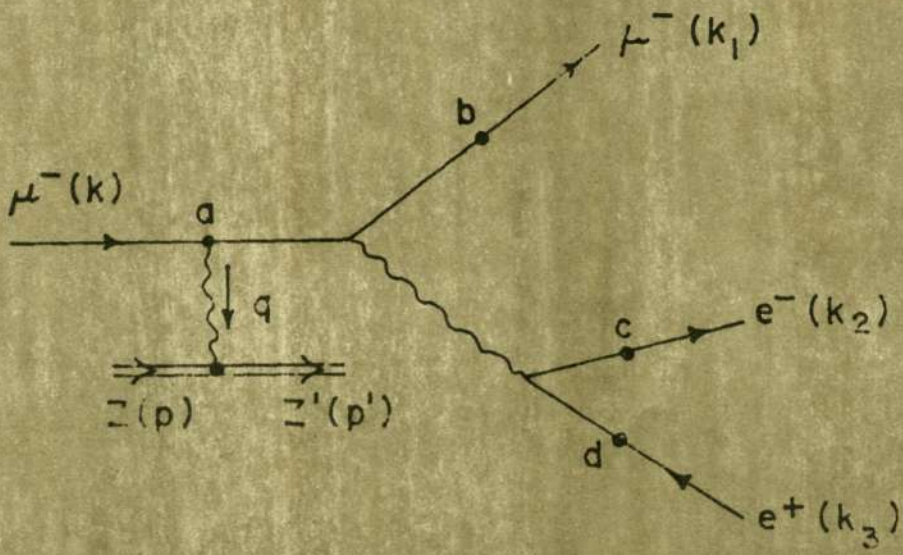

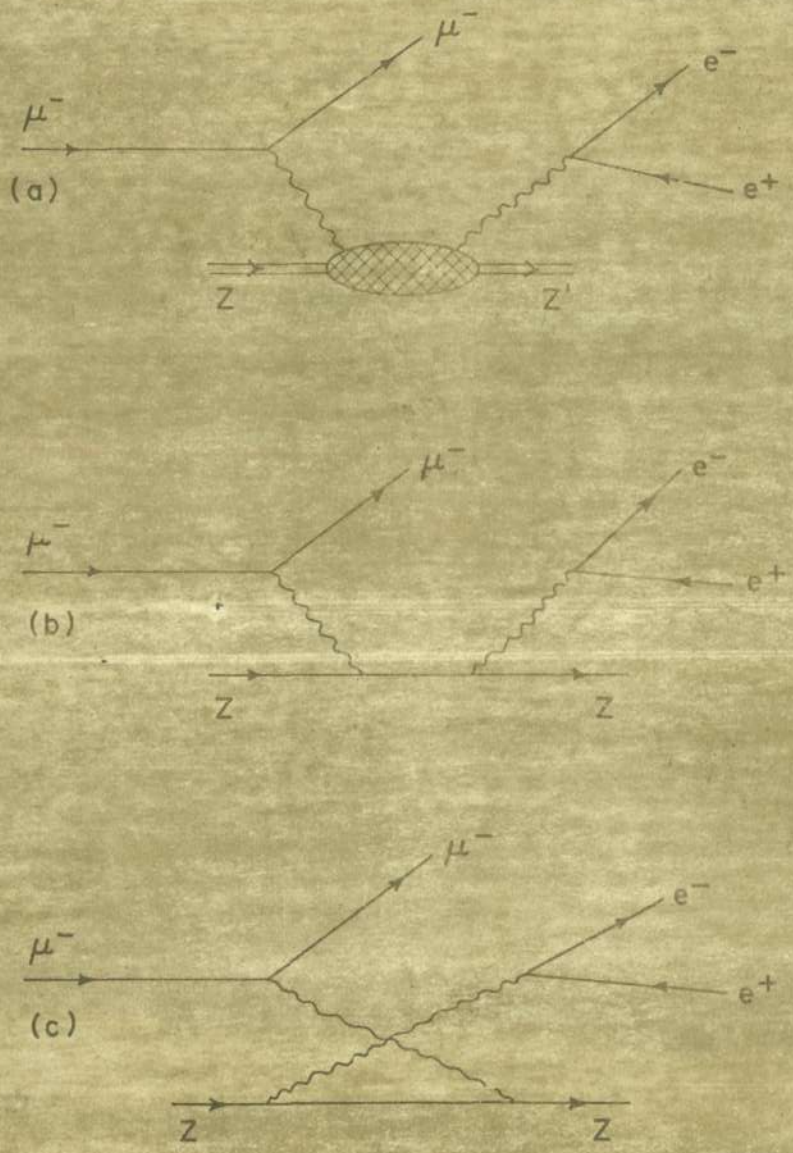
μ⁻
μ⁻
e⁻
e⁺
(a)
Z
Z'
μ⁻
μ⁻
e⁻
e⁺
(b)
Z
Z
μ⁻
μ⁻
e⁻
e⁺
(c)
Z
Z

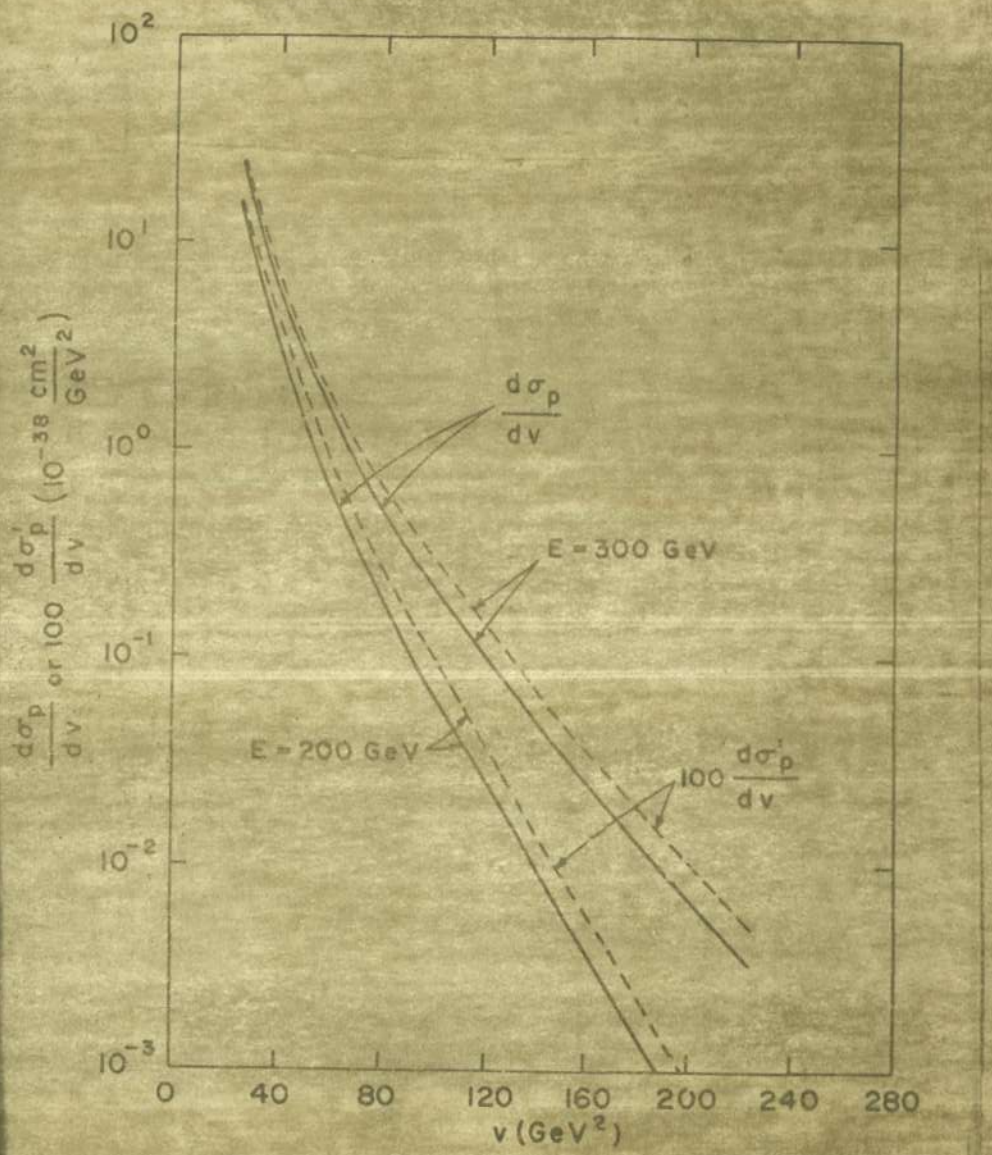
10^2
10^1
10^0
10^{-1}
10^{-2}
10^{-3}
$\frac{d\sigma_p}{dv}$ or 100 $\frac{d\sigma'_p}{dv}$ (10^{-38} $\frac{cm^2}{GeV^2}$)
$\frac{d\sigma_p}{dv}$
E = 300 GeV
E = 200 GeV
100 $\frac{d\sigma'_p}{dv}$
0
40
80
120
160
200
240
280
v (GeV^2)

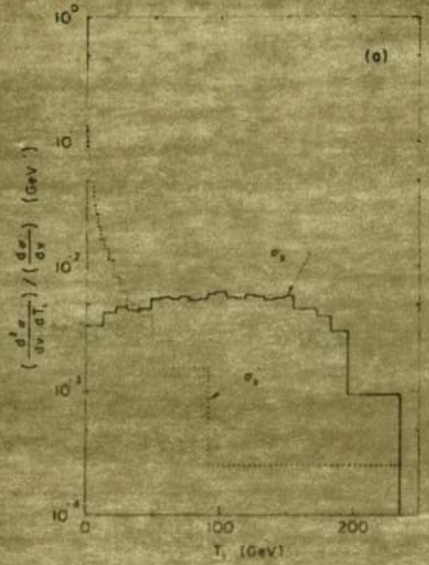
(a)
$\left(\frac{d^2\sigma}{dv\,dT_1}\right)/\left(\frac{d\sigma}{dv}\right)$ (GeV^{-1})
σ_0
σ_0'
T_1 (GeV)


(b)
$\left(\frac{d^2\sigma}{dv\,dT_1}\right)/\left(\frac{d\sigma}{dv}\right)$ (GeV^{-1})
$\sigma_{0,c}$
$\sigma_{0,s}'$
T_1 (GeV)

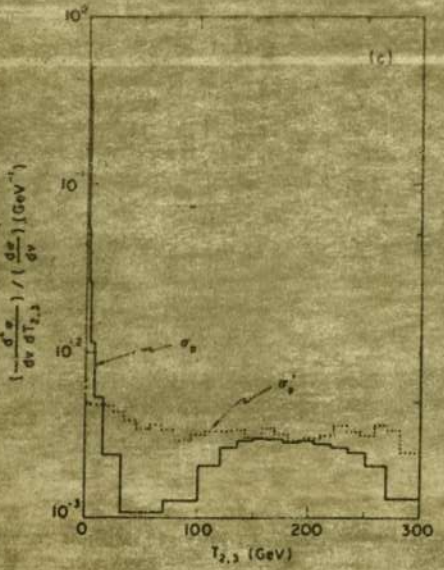
(c)
$\left(\frac{d^2\sigma}{dv\,dT_{2,3}}\right)/\left(\frac{d\sigma}{dv}\right)$ (GeV^{-1})
σ_0
σ_0'
$T_{2,3}$ (GeV)

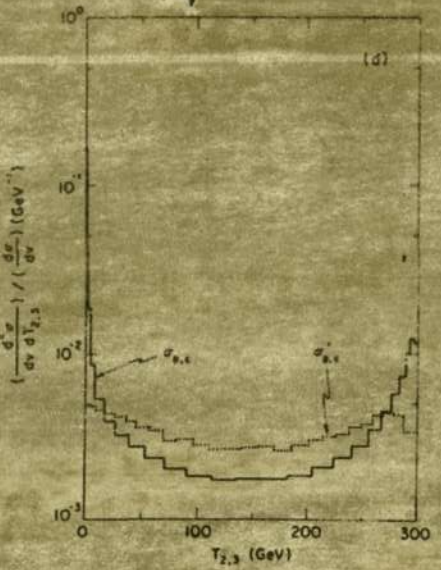
(d)
$\left(\frac{d^2\sigma}{dv\,dT_{2,3}}\right)/\left(\frac{d\sigma}{dv}\right)$ (GeV^{-1})
$\sigma_{0,c}$
$\sigma_{0,s}'$
$T_{2,3}$ (GeV)

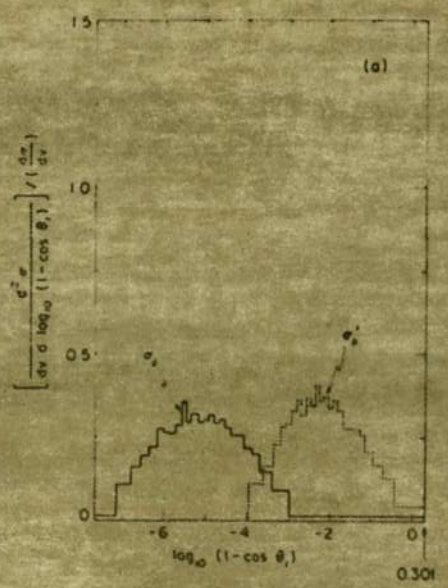
(a)
$\left[\frac{d^2\sigma}{dv\,d\log_{10}(1-\cos\theta_1)}\right]/\left(\frac{d\sigma}{dv}\right)$
σ_0
σ_0'
$\log_{10}(1-\cos\theta_1)$
0.301

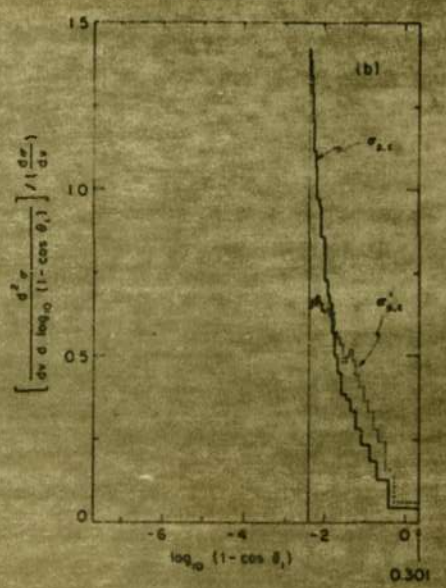
(b)
$\left[\frac{d^2\sigma}{dv\,d\log_{10}(1-\cos\theta_1)}\right]/\left(\frac{d\sigma}{dv}\right)$
$\sigma_{0,c}$
$\sigma_{0,s}'$
$\log_{10}(1-\cos\theta_1)$
0.301

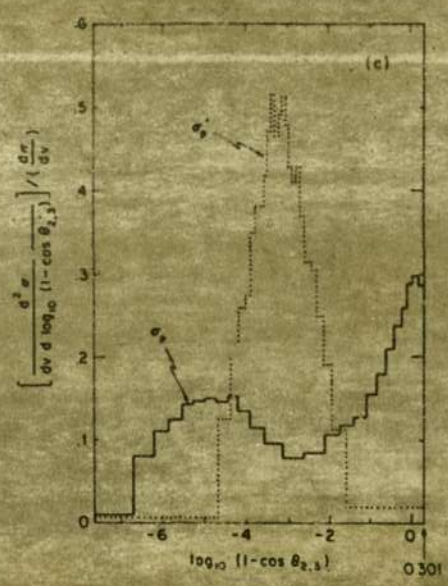
(c)
$\left[\frac{d^2\sigma}{dv\,d\log_{10}(1-\cos\theta_{2,3})}\right]/\left(\frac{d\sigma}{dv}\right)$
σ_0'
σ_0
$\log_{10}(1-\cos\theta_{2,3})$
0.301

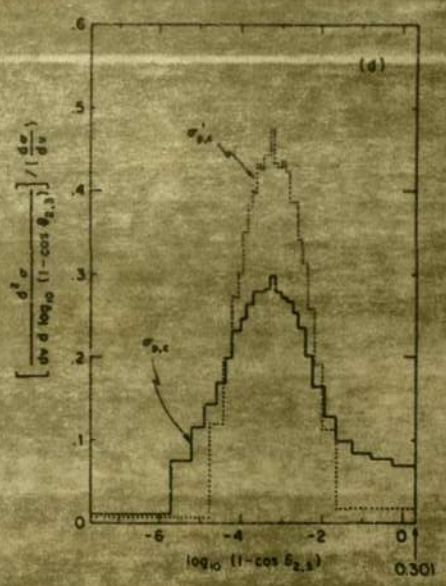
(d)
$\left[\frac{d^2\sigma}{dv\,d\log_{10}(1-\cos\theta_{2,3})}\right]/\left(\frac{d\sigma}{dv}\right)$
$\sigma_{0,s}'$
$\sigma_{0,c}$
$\log_{10}(1-\cos\theta_{2,3})$
0.301


(a)
σ_s
σ_s'
$(\frac{d^2\sigma}{dv\,dk_{\perp 1}}) / (\frac{d\sigma}{dv})$ (GeV^{-1})
$k_{\perp 1}$ (GeV)

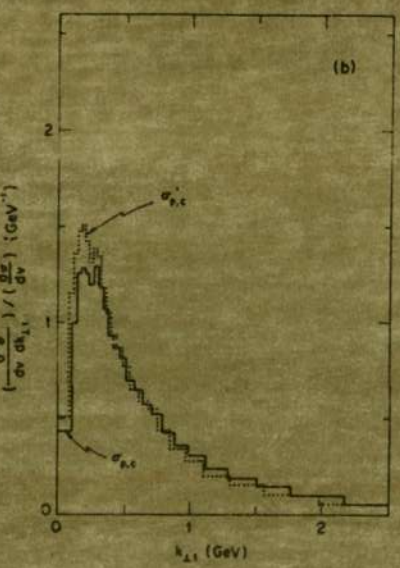
(b)
$\sigma_{s,c}'$
$\sigma_{s,c}$
$(\frac{d^2\sigma}{dv\,dk_{\perp 1}}) / (\frac{d\sigma}{dv})$ (GeV^{-1})
$k_{\perp 1}$ (GeV)

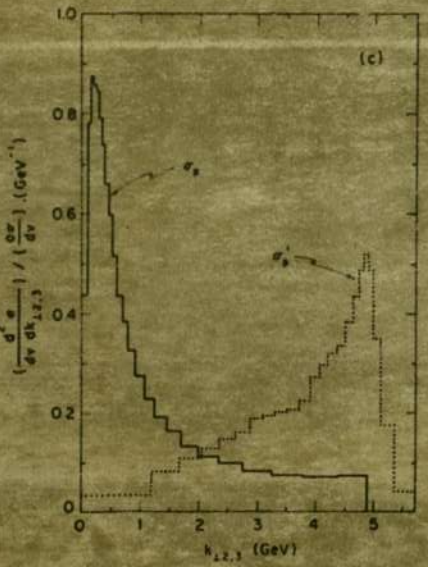
(c)
σ_s
σ_s'
$(\frac{d^2\sigma}{dv\,dk_{\perp 2,3}}) / (\frac{d\sigma}{dv})$ (GeV^{-1})
$k_{\perp 2,3}$ (GeV)

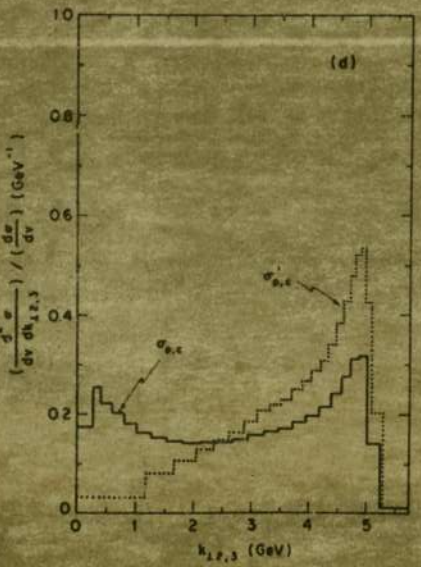
(d)
$\sigma_{s,c}'$
$\sigma_{s,c}$
$(\frac{d^2\sigma}{dv\,dk_{\perp 2,3}}) / (\frac{d\sigma}{dv})$ (GeV^{-1})
$k_{\perp 2,3}$ (GeV)

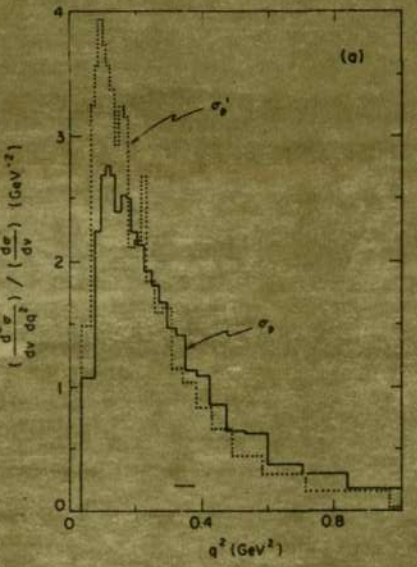
(a)
σ_s'
σ_s
$(\frac{d^2\sigma}{dv\,dq^2}) / (\frac{d\sigma}{dv})$ (GeV^{-2})
q^2 (GeV^2)

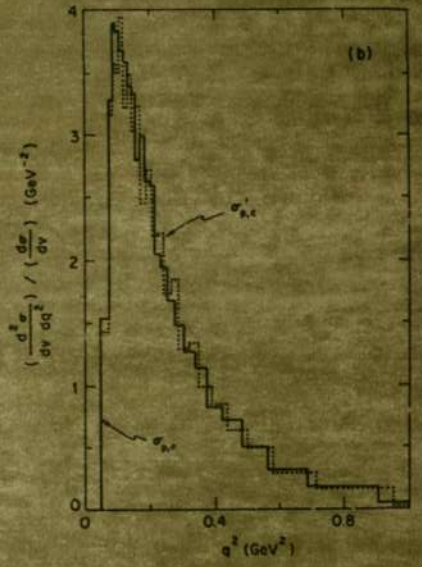
(b)
$\sigma_{s,c}'$
$\sigma_{s,c}$
$(\frac{d^2\sigma}{dv\,dq^2}) / (\frac{d\sigma}{dv})$ (GeV^{-2})
q^2 (GeV^2)

END

DATE FILMED

3 / 6 / 72